China Geology 7 (2024) 237−247

China Geology

Journal homepage: http://chinageology.cgs.cn
https://www.sciencedirect.com/journal/china-geology

Airblast evolution initiated by Wangjiayan landslides in the M_s 8.0 Wenchuan earthquake and its destructive capacity analysis

Yu-feng Wang[a,*], Qian-gong Cheng[a], Qi Zhu[b]

[a] *Department of Geological Engineering, Southwest Jiaotong University, Chengdu* 610031, *China*
[b] *Sichuan Highway Planning, Survey, Design and Research Institute Ltd, Chengdu* 610041, *China*

ARTICLE INFO

Article history:
Received 26 December 2023
Received in revised form 7 March 2024
Accepted 11 March 2024
Available online 24 April 2024

Keywords:
Landslide
Voellmy rheological law
3D FLUENT simulation
Airblast
Intensity
Building destructive collapse
Wenchuan earthquake
Geological hazards survey engineering

ABSTRACT

Airblasts, as one common phenomenon accompanied by rapid movements of landslides or rock/snow avalanches, commonly result in catastrophic damages and are attracting more and more scientific attention. To quantitatively analyze the intensity of airblast initiated by landslides, the Wangjiayan landslide, occurred in the Wenchuan earthquake, is selected here with the landslide propagation and airblast evolution being studied using FLUENT by introducing the Voellmy rheological law. The results reveal that: (1) For the Wangjiayan landslide, its whole travelling duration is only 12 s with its maximum velocity reaching 36 m/s at t=10 s; (2) corresponding to the landslide propagation, the maximum velocity, 28 m/s, of the airblast initiated by the landslide also appears at t=10 s with its maximum pressure reaching 594.8 Pa, which is equivalent to violent storm; (3) under the attack of airblast, the load suffered by buildings in the airblast zone increases to 1300 Pa at t=9.4 s and sharply decreased to –7000 Pa as the rapid decrease of the velocity of the sliding mass at t=10 s, which is seriously unfavorable for buildings and might be the key reason for the destructive collapse of buildings in the airblast zone of the Wangjiayan landslide.

1. Introduction

Airblast, generated in the extremely rapid travel of landslides or rock/snow avalanches, usually present devastating capacity, which can wipe out a whole forest in a minute, or buffet lighter houses before it or blow away people. This phenomenon has been reported in many landslides or rock avalanches with proves, liking directional bent or toppled trees, uprooted trees, mud spatters, tumbled car, etc., deposited along their travelling paths (Heim A, 1932; Kiersch GA, 1964; Fahnestock RK, 1978; Mathews WH and McTaggart KC, 1978; Plafker G and Ericksen GE, 1978; Voight B, 1978; Jiang Y et al., 1991; Cruden DM and Lu ZY, 1992; Morrissey MM et al., 1999; Wieczorek GF et al., 2000; Erismann TH and Abele G, 2001; Catane SG et al., 2008; Cheng QG et al., 2012; Xu Q et al., 2012; Kargel JS et al., 2015). One notable case is the airblast caused by the 1996 Happy Isles rockfall in the Yosemite National Park, U.S.A with its velocity exceeding 110 m/s, which toppled or snapped about 1000 trees immediately downslope of the impact of the rockfall (Morrissey MM et al., 1999; Wieczorek GF et al., 2000). Along the travelling path of the Langtang rock avalanche triggered by the 2015 Gorkha earthquake in Nepal, powerful airblast was also generated with the wind speed comparable with an EF5 tornado (Kargel JS et al., 2016). However, due to the airblast is initiated by the high speed movement of avalanche masses and will disappear rapidly in the accumulation process, there is almost no recorded data on its evolution instead of some indirect proves, liking directional toppled trees and buildings. Additionally, although such phenomenon has been reported in many cases, detailed descriptions on it are limited (Penna IM et al., 2021). The lacking of data on airblast greatly prevents the study on its dynamics.

Based on the TORRO Tornado Intensity scale, the maximum values of the airblasts generated by the Happy Isles collapses were roughly conducted by Wieczorek GF et al. (2000), which is near to the simulated values conducted by

First author: *E-mail address*: wangyufeng@swjtu.edu.cn (Yu-feng Wang).

* Corresponding author: *E-mail address*: wangyufeng@swjtu.edu.cn (Yu-feng Wang).

Literary editor: Li-qiong Jia
doi:10.31035/cg2023154
2096-5192/© 2024 China Geology Editorial Office.

Morrissey MM et al. (1999). In the field of powder snow avalanches, simplified calculations on airblast velocity and height have also been conducted based on the data recorded by photogrammetric and videogrammetric methods (Dreier L et al. 2016). Using the TORRO scale, estimations on the airblast velocities of several landslides have also been conducted by Penna IM et al. (2021) with the slope conditions meeting to trigger a significant airblast being discussed. Additionally, simulations and work on back-analysis of the avalanche airblast intensity have also been primarily conducted in recent years (Zhuang Y et al., 2019, 2023a, 2023b). Although much work has been conducted on the dynamics and potential runout of large rapid slope collapses, very few studies have been carried out on airblast with its velocity evolution and destructive capacity still unclear due to lacking enough geological support.

During the Wenchuan earthquake occurred on May 12, 2008, Sichuan Province, China, more than ten of landslides and rock avalanches travelled with intensive airblasts, especially for the Wangjiayan landslide (WJYRS) located at the Beichuan County (Tang HM et al., 2010; Yin YP et al., 2011). It is reported that airblast, created by the rapidly travelling mass of the WJYRS, extended for a maximum distance of 70 m around the main sliding mass, with many of buildings collapsed in an echelon alignment and parallel to the moving direction of the landslide (Yin YP et al., 2011). Additionally, there are over 20 people, who were working at the toe of the slope, survived and they recalled that they were lifted up in front of the rapid moving mass, transported and then let down gently on the ground safely. The abundant field evidence and detailed narrations of the survivors provide valuable data on the back-analysis of the airblast initiated by the WJYRS. Therefore, a further quantitative study on the dynamics of the airblast initiated by the WJYRS is conducted here, hoping to provide more insights into the evolution of airblast related to rock slope collapses and give suitable risk assessments for the planning development of mountainous areas. Aiming at the purpose, the geological setting of the WJYRS is introduced firstly. After then, the numerical method used in this analysis is presented briefly. Finally, the variation of the airblast created by the rapidly travelling mass is described quantitatively with its devastating capacity being analysed.

2. Wangjiayan landslide

2.1. Geological setting

The WJYRS is detached from a steep slope in the west part of the old Beichuan County in Sichuan Province, China on May 12, 2008 (Fig. 1). It is one of the most serious geological disasters occurred during the Wenchuan earthquake, burying about 1600 people and destroying hundreds of houses (Yin YP et al., 2009; Cui P et al., 2011; Dai FC et al., 2011). As shown in Fig. 1b, the slope angle of the WJYRS mainly ranges from 30° to 50° with the slope orientation being N70°E. The elevations of the landslide crown and deposit toe are 1000 m and 650 m above sea level (a.s.l.), respectively, giving a height difference of nearly 350 m (Fig. 2). The bedrock in the studied area is mainly composed of weathered sandy shale and siltstone intercalated with laminated sandy slate of the Qingping formation of the Lower Cambrian (ϵ_{1c}), covered by Quaternary eluviums of fragmented rocks and soils (Q_4^{el}) (Fig. 2). The bedding plane of the bedrock mainly dips at 35° towards N10°W, which intersects with the slope nearly perpendicularly. At the toe of the slope, it is the display of thick debris flow deposit, consisting of boulders, gravels, sands and silty clay (Q_4^{sef}) (Fig. 2).

2.2. Main deposit characteristics

The WJYRS extends a length of about 700 m with its

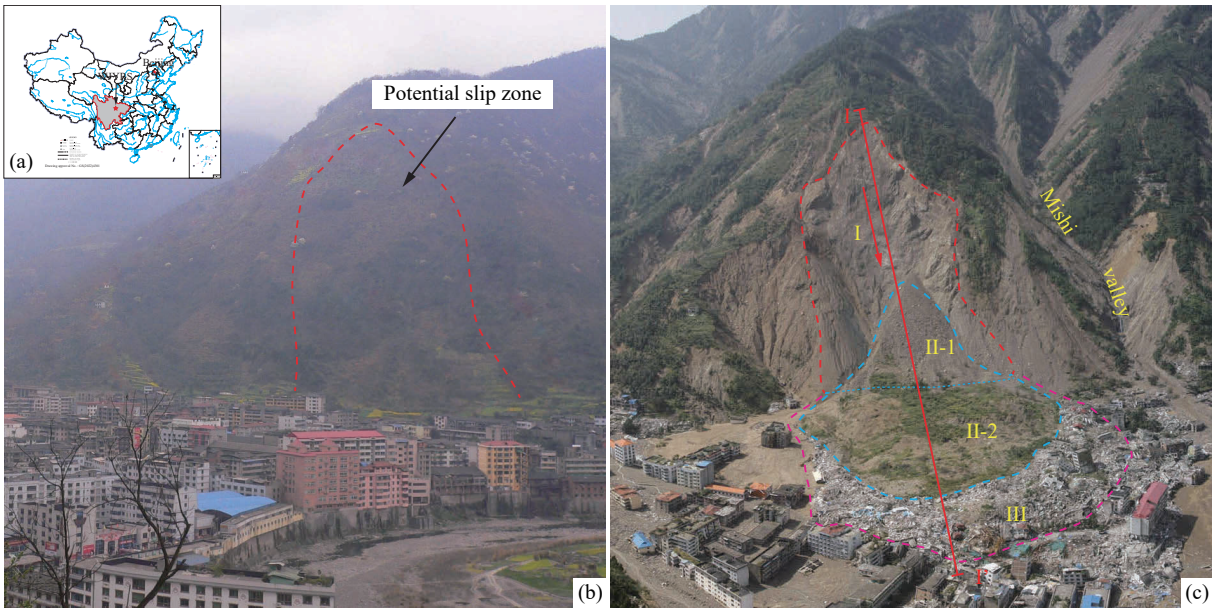

Fig. 1. Location map of the Wangjiayan landslide (a) with the photos of its pre- (b) and post-sliding (c).

maximum width being 280 m. The maximum thickness of the deposit is 35 m. Through a comparison of the pre- and post-topography, it is calculated that the volume of the landslide is about 1.4×10^6 m^3. According to the longitudinal features of the landslide, it can be divided into three zones: The source area (Zone I), the accumulation zone (Zone II), and the airblast zone (Zone III) (Figs. 1c, 2). The characteristics of each zone are described as follows.

2.2.1. Source area (Zone I)

As shown in Fig. 1, the landslide was initiated from the front steep slope of an isolated mountain ridge in the west part of the old Beichuan County, with its elevation ranging from 720 m to 1000 m a.s.l., mainly composing of intensely weathered sandy shale and siltstone intercalated with laminated sandy slate of the Qingping formation of the Lower Cambrian (ϵ_{1c}) (Fig. 2). After the failure, a U-shaped head scarp, consisting of bedrock of the Qingping formation (ϵ_{1c}), is exposed (Fig. 1c) with its length and an averaged width being 220–250 m and 210 m, respectively. The slope gradient of the exposed head scarp mainly ranges from 44° to 55° with a convex shape in longitudinal profile (Fig. 2).

2.2.2. Accumulation zone (Zone II)

The accumulation zone is about 380 m long and 230 m wide in plane. According to the variation of the deposit morphology, it can be sub-divided into two sub-zones (Fig. 1c). The upper sub-zone II–1 is present in a triangle shape, accumulated at the lower part of the steep slope, with its maximum length and width being 160 m and 230 m, respectively. Around 10^5 m^3 of debris is deposited in this sub-zone, with a maximum thickness of 10 m, mainly consisting of intensely weathered gray to grayish yellow coarse blocks and gravels. Due to the control of the underlying steep sliding surface, the slope gradient of the deposit in this sub-zone is high, mainly ranging from 30° to 40°. The lower sub-zone II–2 is the main accumulation area of the sliding mass, exhibiting an oval shape in plan with a maximum length of 220 m, a maximum width of 230 m, and an averaged thickness of 28 m. In this sub-zone, a volume of 1.39×10^6 m^3 of debris is kept, which mainly consists of intensely weathered gray to grayish yellow blocks, gravels, and soil. The slope gradient of the deposit in this sub-zone is gentle that mainly ranges from 10° to 20°. Fig. 3 shows the deposited features in subzone II–2 with the original stratigraphy of the bedrock being preserved, indicating a low disturbance of the mass during the high speed movement.

2.2.3. Airblast zone (Zone III)

Greatly different from the deposited characteristics of sub-

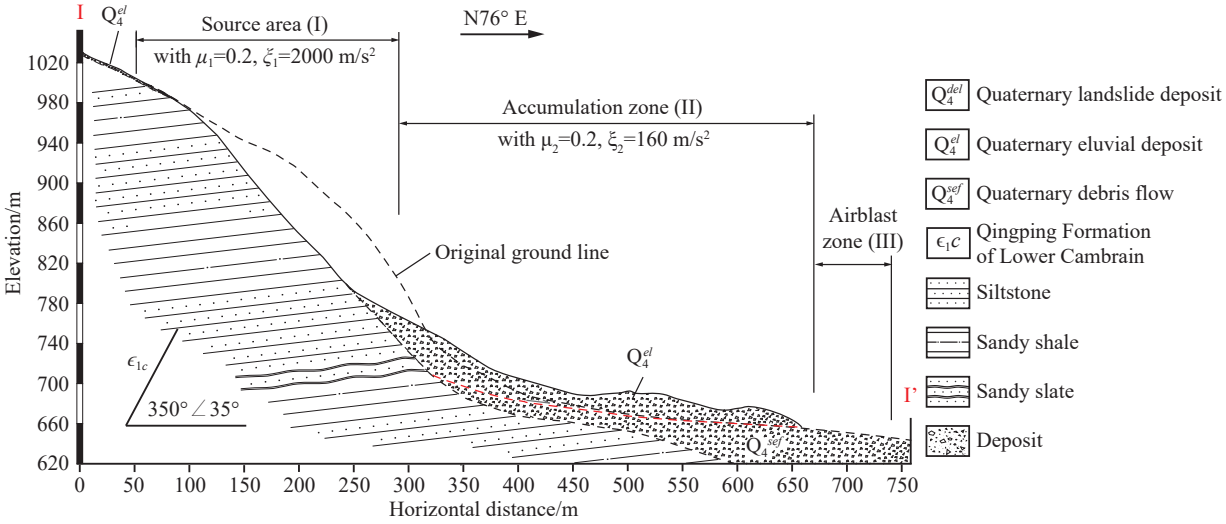

Fig. 2. Longitudinal profile I–I' of the Wangjiayan landslide with the location of I–I' marked in Fig. 1c.

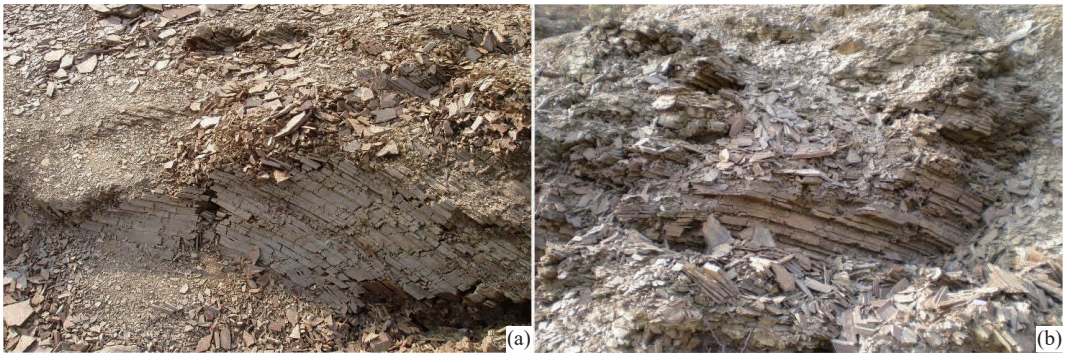

Fig. 3. Photos of the preserved stratigraphy in subzone II–2.

zone II–2, a crescent-shaped zone (zone III) mainly featured by severe collapsed buildings can be observed beyond sub-zone II–2 (Fig. 4). As observed during field investigation, the amount of landslide debris in this zone is scarce with few scattered clasts distributed on the surface of rubbles (Figs. 4b–d), which indicates that the influence of the sliding mass in this zone is limited. But, buildings in this zone are completely collapsed with most collapsed rubbles present in directional alignment and parallel to the landslide moving direction (Fig. 4b), indicating that another force instead of earthquake shaking should be contributed to the collapse and directional alignments of buildings in zone III. Beyond zone III, buildings still stand without collapse although they have been damaged by strong earthquake shaking. Survivors at the foot of the landslide mentioned that accompanied with the rapid motion of the sliding mass, a heavy dust cloud was generated ahead of the mass. And over 20 people, who were working at the toe of the slope, were lucky enough to have been transported outside of the sliding mass to be deposited on the ground safely. Similar phenomena have also been observed in other extremely rapid landslides or rock/snow avalanches (Heim A, 1932; Cruden DM and Lu ZY, 1992; Morrissey MM et al., 1999; Wieczorek GF et al., 2000; Cheng QG et al., 2012). Therefore, according to the features of this zone, airblast zone was used here to name it. The airblast zone, initiated by the Wangjiayan landslide, extends for an averaged distance of 40 m around the sliding mass.

3. Dynamic model designed in FLUENT

To learn the dynamics of the airblast initiated in the rapid motion of the WJYRS, the FLUENT software is used here for its advantage in fluid simulation. FLUENT, as one kind of commercial software launched in 1983, has been widely used in the fields of aerospace, automobile design, multiphase flow, etc., for its advantages in the simulation of complex fluid motion and thermal conduction. Furthermore, it also provides a friendly second-development interface based on C/C++ language, offering great convenience for users. That is why we select FLUENT in this study to simulate the evolution of the airblast created in the extremely rapid motion of the WJYRS.

3.1. Model setup

According to the topographic maps of the pre- and post-event, a three dimensional model used for calculation in FLUENT was generated with its length 930 m, width 600 m, and height 1700 m, which is broader than the landslide scale to eliminate boundary effect (Fig. 5a). The areas numbered with ① and ② are the source area and ground beyond the source area, respectively. The area numbered with ③ is the scope where gas distributes. Referring to the structures and distributions of these collapsed buildings existed in the airblast zone before the failure of the landslide (Fig. 1b), seven rigid buildings (labelled with a to g) were built in this model with some pressure monitoring points being arranged to learn the evolution of airblast intensity after reaching buildings (Fig. 5).

Considering the low disturbance of the sliding mass in propagation and the homogeneity of the detached rock mass in physical and mechanical properties, the detailed composition of the detached mass is neglected and an "equivalent fluid" governed by simple rheological

Fig. 4. Photos show the display of buildings around the Wangjiayan landslide (a) with enlarged views to show the deposited features of the collapsed buildings in the airblast zone (b–d).

relationships (Hungr O, 1995) is considered here. The failure mechanism is neglected here with an initial velocity v_0=3 m/s being designed based on a series of back-analyses considering of the release of strain energy accumulated along the sliding surface during the failure process. Meanwhile, it is assumed that the motion of the landslide takes place in a relatively short time (compared to the total duration) after failure. Based on the above assumptions, the sliding mass in the source area (zone ①) is defined as a liquid with its bulk density 2.1 g/cm^3. For the determination of the bulk density, a sand cone method was used in our field investigation with three sites near the source area being tested and an averaged value 2.1 g/cm^3 being reached. Considering that the pre-landslide air pressure of the studied area is 1 atmosphere (atm), the physical properties of air under 1 atm were designed as the initial values of gas in zone ③ and the *k*-*ε* turbulence model is selected in this study. For the boundary conditions, the area of zone ② is set as the wall without heat flux and the other sides of the model are set as the pressure outlets. Table 1 and Table 2 are the list of the detailed information of the physical properties of the materials and convergence criteria, respectively. In Table 1, the physical properties of gas were determined referring to the empirical values of air at 1 atm and room temperature conditions.

3.2. Rheological law improvement

Considering the flow-like characteristic and low disturbance of the sliding mass in its high movement, a Voellmy rheological law is written into FLUENT through its second-development interface to define the basal shear stress of the sliding mass, which can reproduce the motion of such catastrophic gravity driven flow-like materials ideally (Hungr O, 1995; Crosta GB et al., 2004). The following is the equation defining the basal shear stress as a function of a frictional and a turbulent term in the Voellmy rheological model (Sosio R et al., 2008):

$$\tau = \sigma\mu + \frac{\rho g \upsilon^2}{\xi}, \tag{1}$$

Where τ is the basal shear stress, σ is the normal stress at the base of the sliding mass, μ is the basal frictional coefficient, ρ is the bulk density of the sliding mass, g is the gravitational acceleration, υ is the depth-averaged velocity of the sliding mass, ξ is the turbulent coefficient. From Equ. 1, it can be observed that the frictional term relates the shear stress to the normal stress through a friction coefficient μ. The turbulent term summarizes all velocity-dependent factors of flow resistance, and is expressed by the square of the velocity and the density of the debris through a turbulence coefficient ξ. According to the ranges of the Voellmy rheological parameters argued in literature (Hungr O and Evans SG, 1996, 2004; Chen H and Lee CF, 2003; Pirulli M et al., 2004; McKinnon M et al., 2008; Sosio R et al., 2008; Delaney KB and Evans SG, 2015), back-analyses of the WJYRS were carried out primarily using FLUENT with the validity of the model being assessed through comparisons of the calculated and observed landslide characteristics. Through the back-analyses, it is reached that the best overall simulation is obtained when the Voellmy rheological parameters are

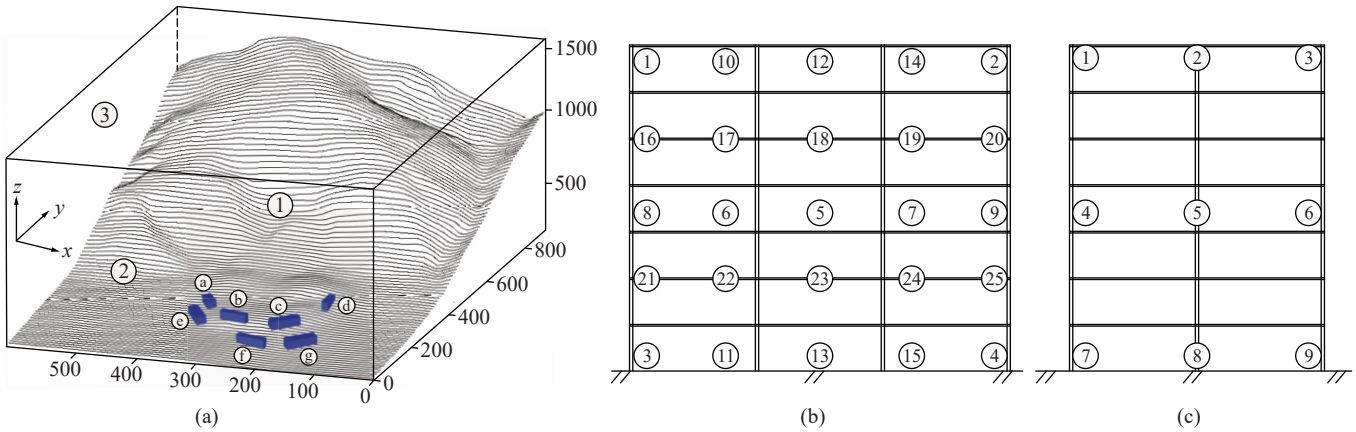

Fig. 5. 3D numerical model of the studied area (a) with the arrangements of the monitoring points on the windward surfaces of the buildings a, c, e, g (b) and b, d, f (c).

Table 1. Physical properties of the materials used in the FLUENT simulation.

Phase type	Material name	Density/(kg/m^3)	Constant-pressure specific heat/[J/(kg·K)]	Thermal conductivity/[W/(m·K)]	Viscosity/[kg/(m·s)]
Gaseous	Air	1.225	1006.43	2.42×10^{-2}	1.79×10^{-5}
Liquid	Landslide mass	2100	–	–	–

Table 2. Convergence criteria used in the FLUENT simulation.

Number of iterations	Convergence criteria				
	Continuity	X-velocity/(m/s)	Y-velocity/(m/s)	Turbulent kinetic energy /(*k*/J)	Turbulent dissipation rate (*ε*/%)
11300	0.001	0.001	0.001	0.001	0.001

$\mu_1 = 0.2$, $\xi_1 = 2{,}000\ \mathrm{m/s^2}$ in the upper steep part of the travelling path (i.e., source area) and $\mu_2 = 0.2$, $\xi_2 = 160\ \mathrm{m/s^2}$ in the lower gentle part (i.e., accumulation zone), respectively.

4. Results

4.1. Propagation of the Wangjiayan landslide

Fig. 6 exhibits the geomorphologic and debris thickness evolutions of the siding mass to provide a clearer understanding of the shape evolution of the sliding mass. Meanwhile, a series of frames showing the velocity evolution of the sliding mass in spatial and time are exhibited in Fig. 7. From Fig. 6 and Fig. 7, several typical and interesting moments of the sliding mass are noticed. It is reached that the whole travel time of the sliding mass is about 12 s. At the very beginning of the failure, the thickest point of the sliding mass is in the rear part with its value exceeding 70 m. After detaching from the source area, the failed mass slid down the slope under gravity and deformed with obvious transversal spreading and the position of the thickest point of the sliding mass moves forward with its value decreasing gradually (Figs. 6b–f). From Fig. 6f, it is reached that the thickest area is located in the rear middle part of sub-zone III-2, which is consistent with the thickness variation as revealed in the longitudinal profile. Corresponding to the thickness variation of the sliding mass, the mass velocity displays a spatial

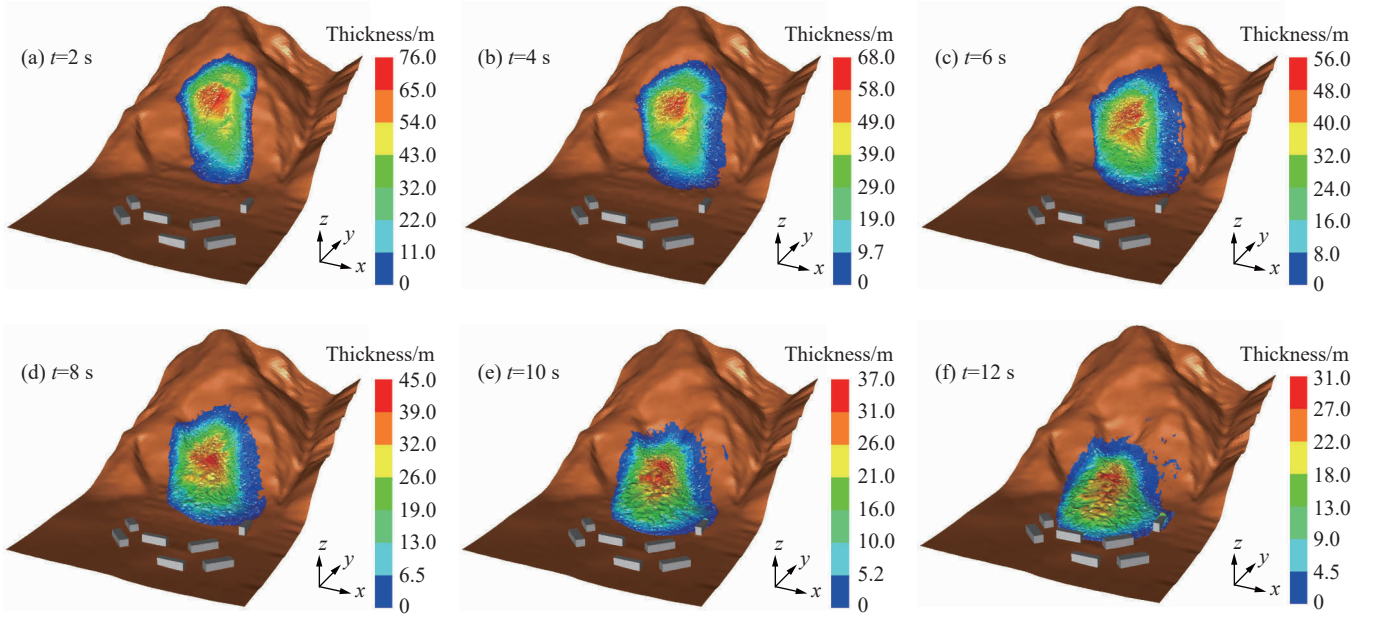

Fig. 6. Snapshots exhibit the geomorphologic and debris thickness evolutions of the sliding mass.

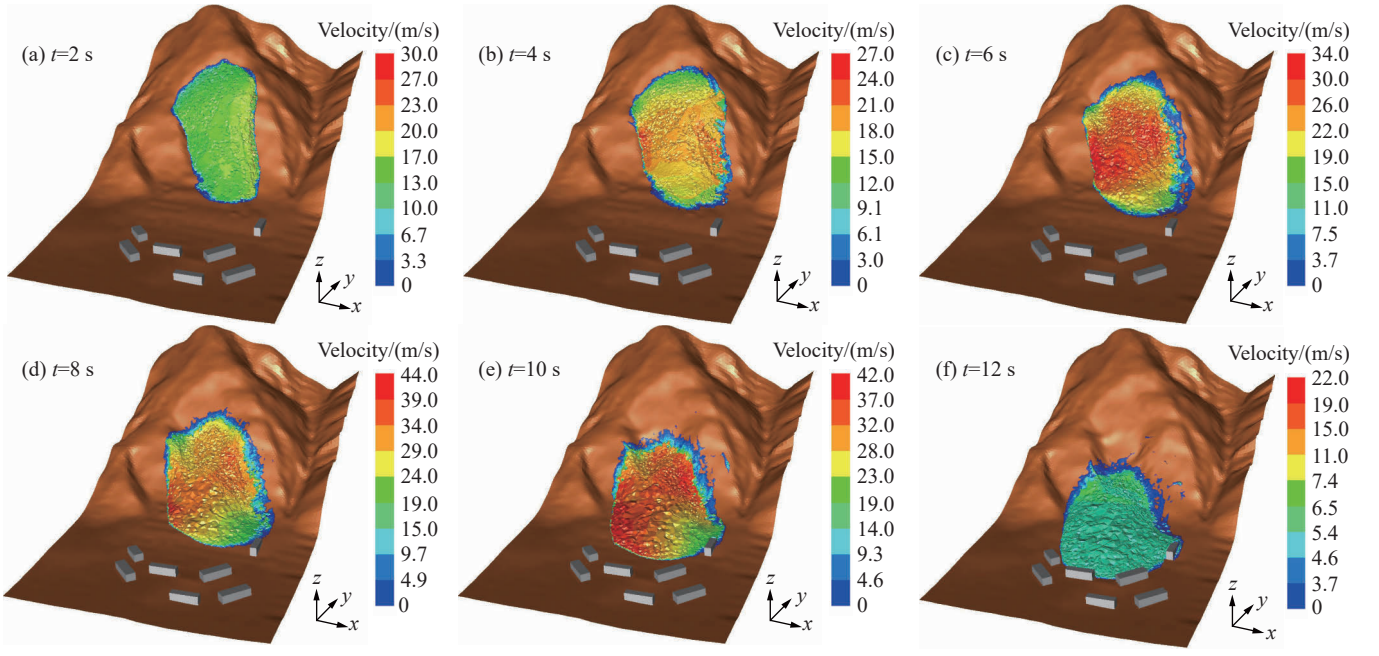

Fig. 7. Snapshots exhibit the velocity variation of the sliding mass.

change with time. In the very beginning, the mass near the left boundary has a relatively high velocity under the control of the topography. With continuous movement, the velocity of the right area increased obviously with the maximum velocity moving forward obviously. And the evolution of the velocity displays a first increasing and then decreasing trend in time with its maximum value mainly distributed in the middle part of the sliding mass (Figs. 7b–f). In the whole propagation, the maximum velocity of the sliding mass appears at t=10 s with its value reaching 36 m/s (Fig. 7e). As reported by survivors, the whole travelling time is no more than 15 s with its maximum speed reaching 30 m/s, which is near to the simulated results presented in Figs. 6 and 7. After t=10 s, a rapid decrease of the mass velocity presents due to the obstruction of the buildings distributed in front of the sliding mass (Fig. 7f).

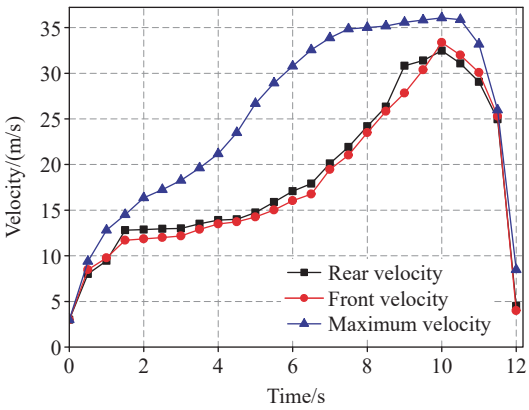

Fig. 8. Time histories of the maximum, front and rear velocities of the sliding mass.

Based on the velocity evolution of the sliding mass, the time histories of the maximum velocity, front velocity and rear velocity of the sliding mass are graphed in Fig. 8. From Fig. 8, it is revealed that, after detaching from the source area, the sliding mass firstly experienced an accelerated motion. At t=10 s, the maximum velocity, front velocity and rear velocity of the sliding mass reached their maximum values of 36 m/s, 33 m/s and 32 m/s, respectively. After the acceleration stage, the velocity of the sliding mass began to decrease rapidly due to more and more debris reached the gentle slope section of the travelling path. When the sliding mass reached the area where buildings distributed at t=11.5 s, a sharp decrease in velocity was reached with the sliding mass almost stopped.

4.2. Airblast evolution initiated by the landslide

Besides the description on the morphological propagation of the sliding mass, the evolution of the airblast created by the rapidly travelling mass is reached here, which is the main purpose of the FLUENT simulation. Fig. 9 shows the variation of the airblast velocity in the vertical and longitudinal directions around the sliding mass. The black line in each subfigure is the boundary between the sliding mass and airblast.

From Fig. 9a, it is observed that, at the initial failure of the mass (t=0.5 s), the airblast is created instantly around the sliding mass with its maximum velocity being 3 m/s. At this moment, the extent and velocity of airblast above the rear part

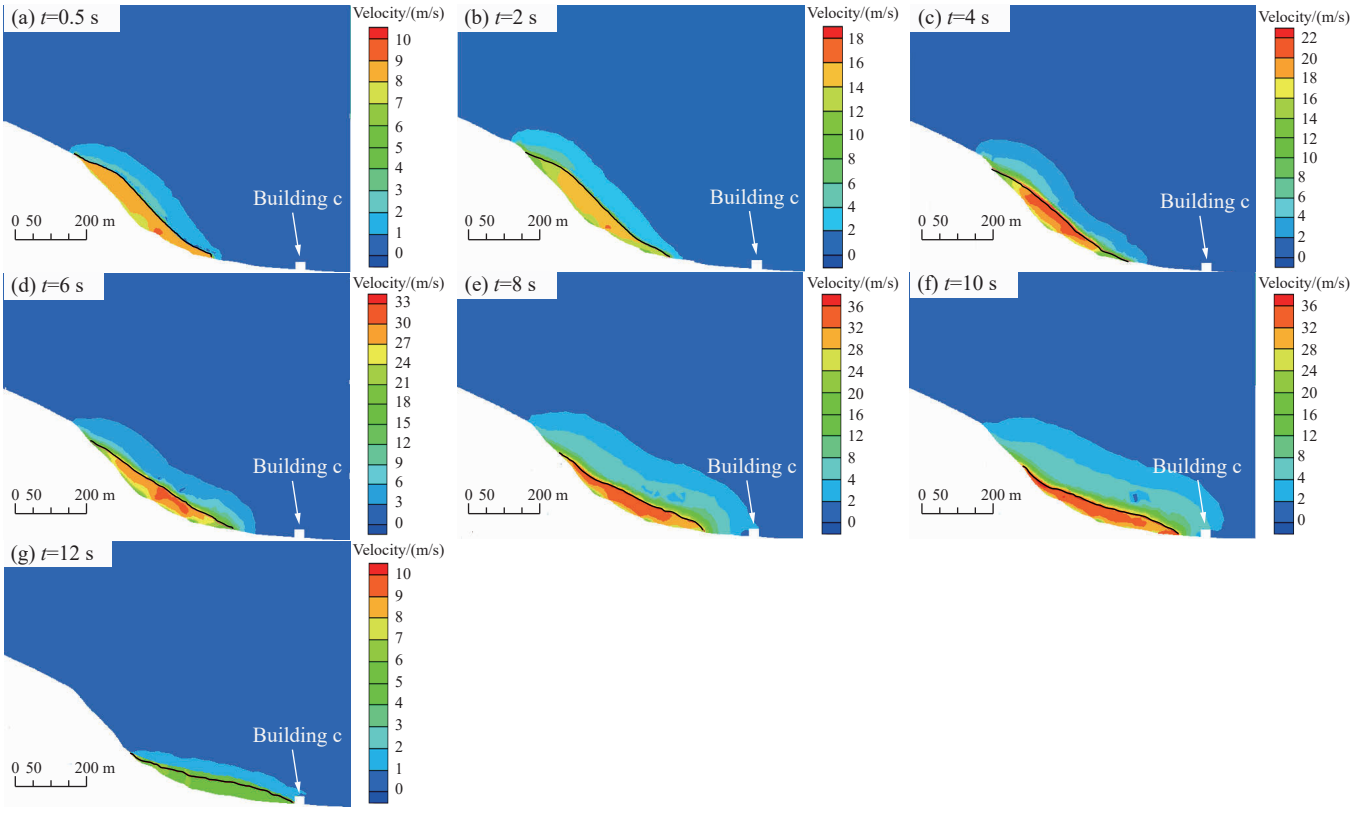

Fig. 9. Snapshots exhibit the velocity variation of airblast.

of the sliding mass are obviously larger than that of the airblast in front of the sliding mass (Fig. 9a). As the downward accelerated motion of the failed mass, the area influenced by airblast began to expand rapidly. And the position where the highest velocity distributed began to move forward as revealed in Figs. 9b–d. At t=8 s, the extension of the airblast in front of the sliding mass reaches 150 m with its maximum velocity being 24 m/s. The windward side and top surface of the building c distributed 125 m away from the sliding mass began to be influenced by airblast (Fig. 9e). With the continued motion of the sliding mass, the extension of the airblast kept to increase in both vertical and longitudinal directions as shown in Fig. 10f with its maximum velocity reaching 28 m/s at t=10 s. At the same time, a small area with lower airblast velocity appears above the front part of the sliding mass (Fig. 9f), which might be formed due to the prevention of buildings. In the following stage, accompanied with the sharply deceleration of the sliding mass, the airblast velocity presents a rapid decrease at t=12 s (Fig. 9g).

Corresponding to the display of the airblast velocity, the evolution of the airblast pressure is shown in Figs. 10a–g with the variation of the airblast pressure ahead of the sliding mass in time and space being graphed in Figs. 10h–i. Here, positive value indicates the pressure is over than 1 atm. From these subfigures, several typical and interesting phenomena are revealed. At $t\leqslant$2 s, the airblast pressure is relatively low and there is almost no change with the motion of the sliding mass as revealed in Figs. 10a−b and Fig. 10h. During this stage, the maximum value of the airblast pressure is only about 250 Pa, which mainly appears around the front part of the sliding mass (Fig. 10b). Near the rear part of the sliding mass, a negative pressure zone appeared with its minimum value reaching −200 Pa (Figs. 10a, b). As the continuous motion of the sliding mass, the distributed pattern of the airblast pressure began to change with a positive pressure zone generated around the rear part of the sliding mass (Fig. 10c). The area with negative pressures decreases and moves to the middle part above the sliding mass with its minimum value being about −70 Pa. With a further increase of runout, the area of the zone with negative pressures increases obviously above the sliding mass with the positive pressure areas focusing in the frontal and rear edges (Figs. 10d–f). At t=8 s, the airblast pressure at the leading edge of the sliding mass reaches 554.4 Pa (Fig. 10e). And within 10 m ahead of the sliding mass, the airblast pressure is also very high with its value over 500 Pa and a great pressure gradient with distance appears (Fig. 10h). As the sliding mass moves forward, the distance between the sliding mass and building c continues to decrease with a maximum airblast pressure, 594.8 Pa, being reached at the leading edge of the sliding mass at t=10 s (Fig. 10h). Meanwhile, a sharp reduction of the airblast pressure at the distance ranging from 60 m to 80 m appears (Fig. 10h), which should be induced by the prevent of the building c. Behind the building c, the airblast pressure tends to stable with its value no more than 100 Pa (Fig. 10h). Corresponding to a rapid decrease of the mass velocity, a negative pressure

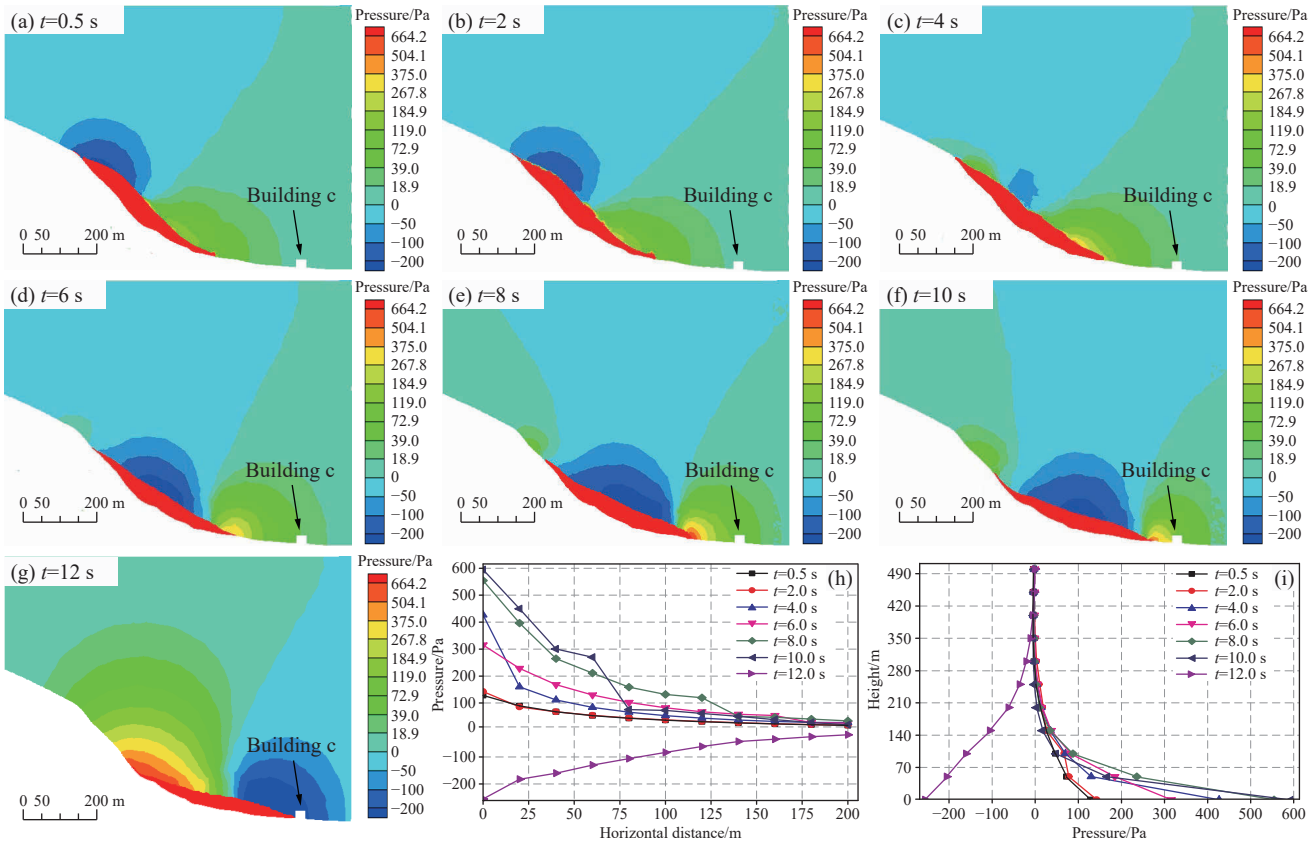

Fig. 10. Snapshots exhibit airblast pressure variation (a–g) with the horizontal (h) and vertical (i) variations of the airblast pressure ahead of the sliding mass versus time being graphed.

zone appears around the front part of the sliding mass with its minimum value being −180 Pa (Figs. 10g–i).

4.3. Airblast pressure loaded on buildings

To learn the airblast effect on buildings, the load variations suffered by the buildings c in the front and f in the rear are recorded and graphed in Fig. 11. It is noticed that, corresponding to the accelerated motion of the sliding mass with t ranging from 0 s to 10 s, the loads suffered by both buildings are positive. And a great increase of pressure loaded on the building c in the front is revealed when t is ranging from 8 s to 10 s, with its maximum pressure, 1300 kPa, appeared at the bottom of the building at t=9.4 s (the curve of the monitoring point 13 in Fig. 11a). In vertical, it is observed that the pressure loaded on the lower part of buildings is much higher than that on the upper part of buildings, such as those of the monitoring points 1, 3 and 8 exhibited in Fig. 11a. Accompanied with the rapid decrease of the velocity of the sliding mass at t=10 s, a sharp decrease of the pressures loaded on the building appears with negative pressures, over −7000 Pa, generated (Fig. 11a). Compare with the load suffered by building c, the load suffered by the building f behind c is obviously low with its values no more than 100 kPa.

5. Discussion

With the help of the FLUENT software, the intensity evolution of the airblast initiated by the WJYRS is studied here in detail. It is reached that the maximum airblast velocity initiated by the WJYRS is about 28 m/s. According to the Beaufort Scale, such wind speed falls into the scale of 10, which can result in garden sheds destroyed, much damage to tiled roofs and chimneys, tress branches twisted or snapped off, tree uprooted, etc. Such scale is very rare on land. Corresponding to the evolution of the airblast velocity, the pressures loaded on the building c at t ranging from 8 s to 10 s is up to 1300 kPa with the stress fluctuation being over 8000 kPa, which is seriously unfavorable for the stability of buildings (Mehta KC, 1984; Ginger J, 2000).

Field investigations reveal that most buildings in the old Beichuan county are brick-concrete structure. Due to the intensive shaking of the Wenchuan earthquake, they have been destroyed seriously with fissures commonly developed. The commonly distributed fissures reduced the stability of the buildings greatly. The Wangjiayan landslide occurred after the main shock of the Wenchuan earthquake with most buildings having been damaged in some degree. So, according to destroyed capacity given in the Beaufort scale, it should be easy for the destroyed buildings to collapse when the high airblast pressure loaded on them. Furthermore, when there is obstacle distributed along the travelling path, extremely high pressure with great pressure gradient versus distance will be generated due to the intensive compression of air between the sliding mass and obstacle. This is further disadvantage for the stability of buildings. Conversely, the airblast pressure behind the obstacle is very low, which is indicated by the pressure loaded on the building f in the rear. The great difference between the pressures suffered by the buildings c and f reveals that buildings in the front row play an important role in the reduction of the airblast and will be intensively destroyed by airblast. Such features of the airblast pressure reached in the simulation display a high consistent with the destroyed phenomenon observed during field investigation. As field investigation revealed buildings in the airblast zone collapsed completely, but those beyond the airblast zone still stand there steadily although fractures are commonly developed under the effect of earthquake shaking.

In addition to the analysis on the airblast velocity and pressure evolutions, as described above, some people at the toe of the slope were lifted up and carried for a long distance. Airborne clasts were observed by them. During our field investigation, scarcely distributed clasts deposited on the surface of the collapsed buildings were also commonly observed in zone III, indicating the airborne emplacement of some clasts. Such phenomena have also been reported in the Elm rock avalanche with the estimated avalanche speed being over 50 m/s. Due to no data about the failure of buildings were recorded during the occurrence of the Wangjiayan landslide. The only data available are the final collapsed phenomena of buildings and some narrations from the survivors. It is difficult to check the stress history suffered by these buildings. Referring to other literature (Heim A, 1932; Penna IM et al., 2021), the airblast intensity initiated by the

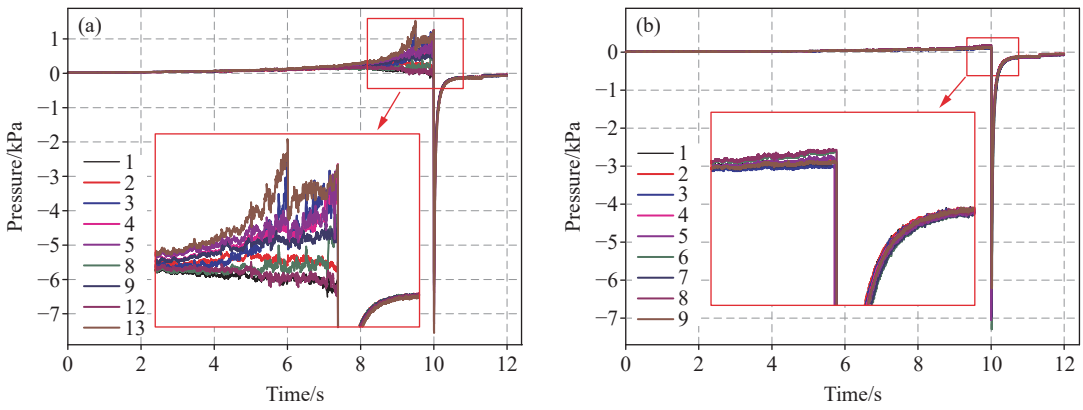

Fig. 11. Pressure evolutions loaded on the monitored points of the buildings c (a) and f (b).

WJYRS might be higher than the simulated results here. Considering the destructive capacity of airblasts in some huge rock collapses, the WJYRS is studied here hoping to gain some insights into the intensity of airblast pressure suffered by buildings and provide useful data for the hazard assessment and sustainable development of mountainous areas. Further study in this field is still needed to explore the potential damage of airblast instead of only considering the landslide hazard and risk assessment.

6. Conclusions

To quantitatively analyze the intensity and devastating capability of airblast initiated in the extremely rapid travel of landslides, the Wangjiayan landslide occurred in the Wenchuan earthquake is studied here with a series of numerical simulations being carried out using FLUENT. With the help of FLUENT, the variation of the airblast created in the rapid motion of the sliding mass is simulated firstly by introducing a Voellmy rheological law. From a comprehensive analysis of these simulated results, some conclusions that may be useful for the study of airblast initiated by landslides or rock/snow avalanches are reached as follows.

(i) For the Wangjiayan landslide, its whole travelling duration lasts about 12 s with its maximum velocity reaching 36 m/s at t=10 s, which are near to the travelling time (no more than 15 s) and maximum velocity (reaching or even exceeding 30 m/s) of the sliding mass estimated from eyewitness descriptions.

(ii) Corresponding to the propagation of the sliding mass, the maximum velocity, 28 m/s, of the airblast initiated by the rapid moving mass also appears at t=10 s with its maximum airblast pressure, 594.8 Pa, being reached at the leading edge of the sliding mass. Within 10 m ahead of the sliding mass, the airblast pressure is very high with its value being over 500 Pa, which is equivalent to violent storm and can induce a devastating destroy to buildings ahead of it.

(iii) Under the attack of airblast, the load suffered by buildings in the airblast zone increased to 1300 Pa at t=9.4 s and sharply decreased to −7000 Pa as the rapid decrease of the velocity of the sliding mass at t=10 s, which is seriously disadvantage for buildings and might be the key reason for the destructive collapse of buildings in the airblast zone of the Wangjiayan landslide.

CRediT authorship contribution statement

Yu-feng Wang carried out the design of this numerical study and finished the draft of the manuscript. Qian-gong Cheng also designed this numerical study and improved the manuscript. Qi Zhu was contributed to the design of this study, and the analysis and interpretation of the data.

Declaration of competing interest

The authors declare that they have no conflict of interests.

Acknowledgements

This research is supported by the National Natural Science Foundation of China (42322702 and 42177131).

References

Catane SG, Cabria HB, Zarco MAH, Saturay Jr RM, Mirasol-Robert AA. 2008. The 17 February 2006 Guinsaugon rock slide-debris avalanche, Southern Leyte, Philippines: Deposit characteristics and failure mechanism. Bulletin of Engineering Geology and the Environment, 67, 305–320. doi: 10.1007/s10064-008-0120-y.

Chen H, Lee CF. 2003. A dynamic model for rainfall-induced landslides on natural slopes. Geomorphology, 51(4), 269–288. doi: 10.1016/S0169-555X(02)00224-6.

Cheng QG, Wang YF, Zhu Q. 2012. Airblast generated by rock avalanche. In: Landslides and Engineered Slopes: Protecting Society through Improved Understanding. London, UK, CRC Press, Taylor & Francis Group, 841–848.

Crosta GB, Chen H, Lee CF. 2004. Replay of the 1987 Val Pola Landslide, Italian Alps. Geomorphology, 60(1–2), 127–146. doi: 10.1016/j.geomorph.2003.07.015.

Cruden DM, Lu ZY. 1992. The landslide and debris flow from Mount Cayley, B. C., in June 1984. Canada Geotechnical Journal, 29 (4), 614–626. doi: 10.1139/t92-069.

Cui P, Chen XQ, Zhu YY, Su FH, Wei FQ, Han YS, Liu HJ, Zhuang JQ. 2011. The Wenchuan Earthquake (May 12, 2008), Sichuan Province, China, and resulting geo-hazards. Natural Hazards, 56, 19–36. doi: 10.1007/s11069-009-9392-1.

Dai FC, Xu C, Yao X, Lu L, Tu XB, Gong QM. 2011. Spatial distribution of landslides triggered by the 2008 M_S 8.0 Wenchuan earthquake, China. Journal Asian Earth Sciences, 40(4), 883–895. doi: 10.1016/j.jseaes.2010.04.010.

Delaney KB, Evans SG. 2015. The 2000 Yigong landslide (Tibetan Plateau), landslide-dammed lake and outburst flood: Review, remote sensing analysis, and process modelling. Geomorphology, 246, 377–393. doi: 10.1016/j.geomorph.2015.06.020.

Dreier L, Bühler Y, Ginzler C, Bartelt P. 2016. Comparison of simulated powder snow avalanches with photogrammetric measurements. Annals of Glaciology, 57(71), 371–381. doi: 10.3189/2016aog71a532.

Erismann TH, Abele G. 2001. Dynamics of landslides and rockfalls. Berlin, Springer Berlin, Heidelberg, 316.

Fahnestock RK. 1978. Little Tahoma Peak rockfalls and avalanches, MountRainier, Washington, U. S. A. In: Landslides and Avalanches: Vo. l 1, Natural Phenomena. US, Elsevier, 181–196.

Ginger J. 2000. Internal pressures and cladding net wind loads on full-scale low-rise building. Journal of Structure Engineering, 126(4), 538–543. doi: 10.1061/(ASCE)0733-9445(2000)126:4(538).

Heim A. 1932. Bergsturz und Menschenleben. Zütich: Naturforschenden Gesellschaft. English Translation by SKERNER N A. Landslides and Human Lives. Vancouver: BiTech Publishers Ltd, 1989, 1–195.

Hungr O. 1995. A model for the runout analysis of rapid flow slides, debris flows, and avalanches. Canada Geotechnical Journal, 32(4), 610–623. doi: 10.1139/t95-063.

Hungr O, Evans SG. 1996. Rock avalanche runout prediction using a dynamic model. In: Proceedings of the 7th International Symposium on Landslides. CRC Press, Taylor & Francis Group, Trondheim, NO, 233–238.

Hungr O, Evans SG. 2004. Entrainment of debris in rock avalanches: An analysis of a long run-out mechanism. GSA Bulletin, 116(9–10), 1240–1252. doi: 10.1130/B25362.1.

Jiang Y, Zhao QH, Yan MG. 1991. Xikou mountain landslide-debris flow, China. In: Balkema AA and Rotterdam (eds.), International

symposlum on landslides. Netherlands, 133–138.

Kargel JS, Leonard GJ, Shugar DH, Haritashya UK, Bevington A, Fielding EJ, Fujita K, Geertsema M, Miles ES, Steiner J, Anderson E, Bajracharya S, Bawden GW, Breashears DF, Byers A, Collins B, Dhital MR, Donnellan A, Evans TL, Geai ML, Glasscoe MT, Green D, Gurung DR, Heijenk R, Hilborn A, Hudnut K, Huyck C, Immerzeel WW, Jiang LM, Jibson R, Kääb A, Khanal NR, Kirschbaum D, Kraaijenbrink PDA, Lamsal D, Liu SY, Lv MY, Mckinney D, Nahirnick NK, Nan ZT, Ojha S, Olsenholler J, Painter TH, Pleasants M, Pratima KC, Yuan QI, Raup BH, Regmi D, Rounce DR, Sakai A, Shangguan DH, Shea JM, Shrestha AB, Shukla A, Stumm D, Van der kooij m, Voss K, Wang X, Weihs B, Wolfe D, Wu LZ, Yao XJ, Yoder MR, Young N. 2016. Geomorphic and geologic controls of geohazards induced by Nepal's 2015 Gorkha earthquake. Science, 351 (6269). doi: 10.1126/science.aac8353.

Kiersch GW. 1964. Vaiont reservoir disaster. Civil Engineering, 34, 32–39.

Mathews WH, McTaggart KC. 1978. Hope landslides, British Columbia, Canada. In: Landslides and Avalanches: Vol. 1, Natural Phenomena. US, Elsevier, 259–276.

McKinnon M, Hungr O, McDougall S. 2008. Dynamic analyses of Canadian landslides. In: Proceedings of the Fourth Canadian Conference on GeoHazards: From Causes to Management. Canadian Geotechnical Society, Engineering Geology Division, Presse de l'Université de Laval, CA, 20–24.

Mehta KC. 1984. Wind induced damage observations and their implications to design practice. Engineering Structure, 6(4), 242–247. doi: 10.1016/0141-0296(84)90019-1.

Morrissey MM, Savage WZ, Wieczorek GF. 1999. Air blasts generated from rockfall impacts: Analysis of the 1996 Happy Isles event in Yosemite National Park. Journal of Geophysical Research:Solid Earth, 104(B10), 23189–23198. doi: 10.1029/1999JB900189.

Penna IM, Hermanns RL, Nicolet P, Morken OA, Dehls J, Gupta V, Jaboyedoff M. 2021. Airblasts caused by large slope collapses. GSA Bulletin, 133 (5–6), 939–948. doi: 10.1130/B35531.1.

Pirulli M, Scavia C, Hungr O. 2004. Determination of rock avalanche run-out parameters through back analyses. In: Balkema AA and Rotterdam (eds.), Proceedings of the 9th International Symposium on Landslides. London, UK, 1361–1366.

Plafker G, Ericksen GE. 1978. Nevados Huascaran avalanches, Peru. In: Landslides and Avalanches: Vol. 1, Natural Phenomena. US, Elsevier, 277–314.

Sosio R, Crosta GB, Hungr O. 2008. Complete dynamic modeling calibration for the Thurwieser rock avalanche (Italian Central Alps). Engineering Geology, 100(1–2), 11–26. doi: 10.1016/j.enggeo.2008.02.012.

Tang HM, Jia HB, Hu XL, Li DW, Xiong CR. 2010. Characteristics of landslides induced by the great Wenchuan earthquake. Journal of Earth Science, 21, 104–113. doi: 10.1007/s12583-010-0008-1.

Voight B. 1978. Lower Gros Ventre slide, Wyoming, U. S. A., In: Landslides and Avalanches: Vo. l 1, Natural Phenomena. US, Elsevier, 113–166.

Wieczorek GF, Snyder JB, Waitt RB, Morrissey MM, Uhrhammer RA, Harp EL, Norris RD, Bursik MI, Finewood LG. 2000. Unusual July 10, 1996, rock fall at Happy Isles, Yosemite National Park, California. GSA Bulletin 112(1), 75–85. doi: 10.1130/0016-7606(2000)112<75:UJRFAH>2.0.CO;2.

Xu Q, Shang YJ, Asch TV, Wang ST, Zhang ZY, Dong XJ. 2012. Observations from the large, rapid Yigong landslide-debris avalanche, southeast Tibet. Canada Geotechnical Journal, 49, 589–606. doi: 10.1139/t2012-0.

Yin YP, Wang FW, Sun P. 2009. Landslide hazards triggered by the 2008 Wenchuan earthquake, Sichuan, China. Landslides, 6, 139–152. doi: 10.1007/s10346-009-0148-5.

Yin YP, Zheng WM, Li XC, Sun P, Li B. 2011. Catastrophic landslides associated with the M 8. 0 Wenchuan earthquake. Bulletin of Engineering Geology and the Environment, 70, 15–32. doi: 10.1007/s10064-010-0334-7.

Zhuang Y, Xu Q, Xing AG. 2019. Numerical investigation of the air blast generated by the Wenjia valley rock avalanche in Mianzhu, Sichuan, China. Landslides, 16, 2499–2508. doi: 10.1007/s10346-019-01253-0.

Zhuang Y, Xu Q, Xing AG, Bilal M, Gnyawali KR. 2023a. Catastrophic air blasts triggered by large ice/rock avalanches. Landslide, 20, 53–64. doi: 10.1007/s10346-022-01967-8.

Zhuang Y, Xing AG, Bartelt P, Bilal M, Ding ZW. 2023b. Dynamic response and breakage of trees subject to a landslide-induced air blast: Implications for air blasts risk assessment in mountainous regions. Natural Hazards and Earth System Sciences, 23(4), 1257–1266. doi: 10.5194/nhess-23-1257-2023.